Noname manuscript No.
(will be inserted by the editor)

Architecture for an External Input into a Molecular QCA Circuit

Konrad Walus · Faizal Karim · André Ivanov

Received: date / Accepted: date

Abstract A simple architecture for data input into a molecular quantum-dot cellular automata (QCA) circuit from an external CMOS circuit is proposed. A "T"-shaped interconnect, utilizing fixed-polarization cells to provide the desired polarization, is controlled via external electrodes connected to a standard CMOS input driver. The applied input signal is used to gate either the propagation of a fixed polarization, $P = +1$, or that of the complementary fixed polarization, $P = -1$, into the QCA circuit. The architecture utilizes the field-driven clocking scheme proposed in recent literature to achieve transduction between applied input voltage and a molecular configuration. The system is modelled using the coherence vector formalism with a three-state basis and simulated using the QCADesigner simulation tool.

Keywords Quantum Dot Cellular Automata · QCA · I/O · Molecular computing

1 Introduction

Research into molecular scale electronics has increased significantly over the last decade. One of the proposed paradigms for computing using molecular devices is molecular quantum-dot cellular automata (QCA) [1–3]. Molecular QCA is one of several approaches to molecular electronics, utilizing the electrostatic interactions between the electronic configuration of neighboring molecules to perform computing rather than using the molecule as the channel of a field-effect transistor device. Currently, no complete molecular QCA circuit has been functionally demonstrated and ongoing simulation and experimental research is targeting a variety of molecular structures for implementing the QCA cell [4–9]. Creating functional QCA molecules is just the first step. In a practical device, the molecules require appropriate functionalization for surface attachment, inputs and clocking signals need to be applied, and the state of the output cells must be measured. In addition, some of the molecules should have a fixed polarization in order to use the majority gate to perform AND and OR logic. To date, very little work

K. Walus, F. Karim and A. Ivanov
University of British Columbia, Department of Electrical and Computer Engineering, 2332 Main Mall, Vancouver, BC, Canada V6T 1Z4
E-mail: {konradw,faizalk, ivanov}@ece.ubc.ca

addresses the issue of I/O in molecular QCA and no architectures or devices have been proposed for converting an electrical potential into a QCA polarization in a molecular cell.

In this work, a novel architecture for input into a QCA circuit is proposed. Due to the inherent small size of the molecules, input schemes that have been successfully demonstrated in other implementations of QCA are not applicable. In the proposed architecture, clocking electrodes and cells with fixed polarizations are used to drive the inputs. Both the clocking network and fixed polarization cells are required to support the general functionality of a molecular QCA circuit [10] and are not unique to this particular architecture. As a result, the proposed architecture also minimizes the need for new structures dedicated to the inputs. An additional benefit of this type of driver is that it does not require the QCA interconnects to have a width of only one cell, potentially leading to simplified fabrication.

2 Clocked Molecular QCA

The proposed driver is itself based on a three-state field-clocked implementation of QCA [9, 11–13]. We have taken a high level approach to this problem, modelling the cells using this simple basis in order to provide a proof-of-principle for this input architecture and to enable the analysis of circuit level aspects of its operation. This choice of basis is justified by earlier work that demonstrated that the switching behaviour of molecular QCA can be modelled using this reduced basis [4]. The individual molecular units are modeled using a high-level geometry depicted in Fig. 1. For the molecular QCA cell, three stable electronic configurations are chosen as a basis. Two electronic configurations, in which the mobile charges are located in the top sites of the cell and along one of the two diagonals, represent the ACTIVE states of the cell. In these ACTIVE configurations, the cell is said to have a polarization, $P = \pm 1$. When $P = 1$, the cell is said to represent a binary value of 1, and when $P = -1$, the cell is said to represent a binary value of 0 as shown in Fig. 1. When a cell is in one of the two ACTIVE states, its electrostatic quadrupole-quadrupole interaction with neighboring cells introduces a perturbation that breaks the energy degeneracy of the active states of the neighboring cells and in the ground state configuration, adjacent cells tend to relax to the same ACTIVE state. In the NULL state, where the cell has a polarization, $P = 0$, the mobile charges are located in the bottom sites of the cell. In this configuration, the cell does not break the energy degeneracy of ACTIVE states in neighboring cells. Therefore, cells relax to a polarization that is determined only by neighboring cells for which $P \neq 0$, and this NULL state provides a mechanism for turning cells "off."

Field-driven clocking is possible with a set of electrodes submerged below the layer of cells that generate a near vertical electric field at the level of the QCA molecules [11, 13]. In order to propagate information in such a circuit, phase shifted clocking signals can be applied to consecutive clocking electrodes to create a travelling wave, which drives cells to switch at the wavefront as illustrated in Fig. 2. Here, the signal applied to each of the four electrodes is phase-shifted by ϕ_i as indicated on the electrodes, such that $\phi_1 < \phi_2 < \phi_3 < \phi_4$, creating a right travelling clocking field.

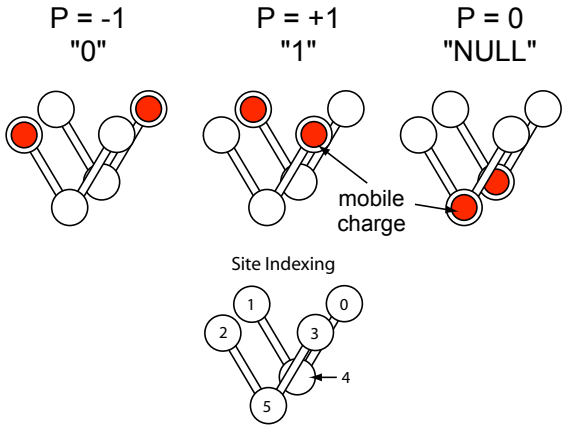

Fig. 1 3-state QCA cells are composed of "V" shaped molecules grouped in pairs. The site indexing used throughout this paper is indicated in the bottom figure.

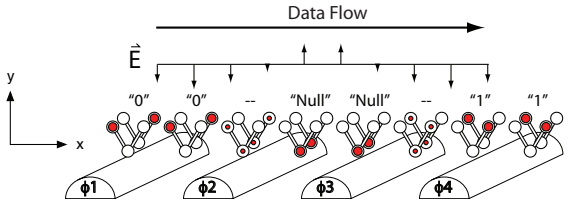

Fig. 2 Schematic depiction of submerged electrodes used to clock a layer of QCA cells by generating a forward moving vertical electric field at the level of the cells. A ground plane located above the cells is not shown in the figure. The illustrated size of the QCA cells are not to scale with respect to the spacing of the electrodes.

3 Proposed Input Driver Architecture

The proposed architecture consists of a structure that will gate the polarization from two clusters of fixed polarization cells into the circuit using the clocking electrodes. A "T"-shaped architecture with clusters of fixed cells connected at two of the ends is shown in the schematic in Fig. 3. A CMOS-based driver and inverter are included to drive the two gating electrodes with complementary signals. The gating electrodes and the QCA cells located directly above them act as a QCA version of a CMOS transmission gate as depicted in the figure. If only one type of fixed polarization cell is available in a particular QCA implementation, similar functionality can be achieved by gating either the signal directly to the output or by gating a second path, which includes a QCA inverter, using a second gate electrode.

The transduction mechanism from CMOS driver to QCA polarization is illustrated in Fig. 4. Here, the two gating electrodes, the first output clocking electrode (E1), and the ground plane are shown. A positive potential has been applied to the electrodes in

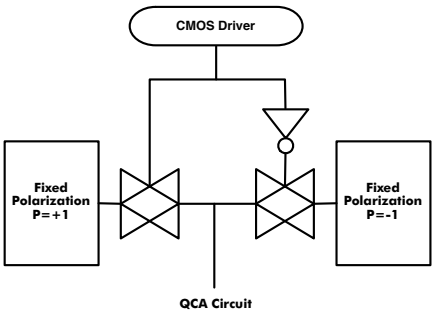

Fig. 3 Schematic of the input driver architecture. A CMOS-based driver and inverter are used to convert the electrical input into a gating potential on two gating electrodes. Depending on the external input, either a polarization of +1 or -1 will be propagated to the QCA circuit.

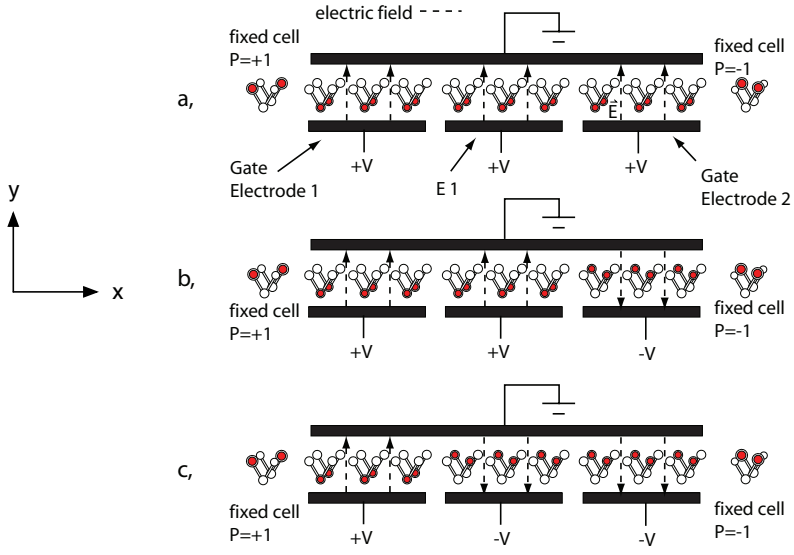

Fig. 4 Transduction mechanism for converting input voltage to cell polarization (assuming anionic molecules). a, with positive applied potentials to all gating electrodes, all the cells will be in the NULL state. b, as the potential on Gate Electrode 2 is switched, the cells in that zone are activated and propagate the polarization, $P = -1$. c, as the potential of E1 switches, the polarization from the gated zone is propagated to the rest of the QCA circuit.

Fig. 4(a). When the applied electric field on the cells in the $\hat{y}$ direction, E_y, is sufficiently large, it will draw the mobile electrons towards the bottom two sites of the cell forcing each cell into the NULL state. During the application of a binary '0' input, the potential on Gate Electrode 2 will turn negative. Once the $\hat{y}$-directed electric field on the cells above this electrode is strongly negative, it will become energetically favorable for the mobile electrons to occupy the upper-sites of the cell. The interaction with the fixed polarized cells to the right will drive these cells into the $P = -1$ polarization (Fig. 4(b)). Lastly, when the applied potential on electrode, E1, switches to a negative voltage, the applied electric field on the cells draw the mobile electrons to the upper-sites of the

cells. The polarization of the cells above Gating Electrode 2 will then be transferred to those above electrode, E1 (Fig. 4(c)). This polarization is then propagated to the output wire via the clocking electrodes of the QCA circuit. The circuit-level operation of the input driver shown in Fig. 3 is depicted in Fig. 5.

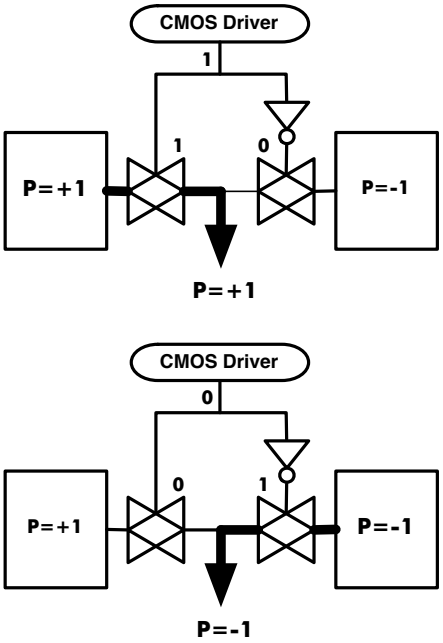

Fig. 5 Schematic depicting the operation of the input driver. A logic '1' energizes the left electrode, propagating a polarization, $P = +1$, to the QCA circuit. A logic '0' energizes the right electrode, propagating a polarization, $P = -1$, to the QCA circuit.

4 Model

A simplified model of the molecular QCA cell (including a cell dynamics solver based on the coherence vector formalism described in [14–17]), was incorporated into the QCADesigner tool [18] to simulate this field-driven molecular implementation. The simulation engine models each QCA cell in the circuit using a three-state Hamiltonian, where the basis functions are the two fully polarized configurations and the NULL configuration. The Hamiltonian is projected onto a basis of generators of the special unitary group $SU(3)$. The resulting Bloch equation is solved to determine the time evolution of the coherence vector in this basis. Interaction with the environment is modeled using a density matrix approach and a relaxation-time approximation. The intercellular Hartree approximation (ICHA) is used to reduce the multi-electron problem and treats the interactions between cells using expectation values.

4.1 Charges

Two fixed positive charges are distributed throughout the cell to ensure that the overall system is charge neutral. This neutralizing charge models the effect of a counter-ion. The location of this counter-ion depends on the details of the physical implementation. As an approximation, the charge from this counter-ion is distributed throughout the cell. The fraction of neutralizing positive charge located in the top four sites of the cell is determined by the parameter $0 \leq \chi \leq 1$. The primary effect of varying χ is a change in the normal cell state, from normally NULL ($\chi = 0$) to normally ACTIVE ($\chi = 1$). For the three basis states, we define the cell charge vector,

$$\mathbf{Q} = [Q_{\text{site }0}, Q_{\text{site }1}, Q_{\text{site }2}, Q_{\text{site }3}, Q_{\text{site }4}, Q_{\text{site }5}], \tag{1}$$

with respect to the indexing shown in Fig. 1. The charge at each site of the cell for the three different basis states is

$$\mathbf{Q}_+ = \left[\chi\frac{e}{2}, \chi\frac{e}{2} - e, \chi\frac{e}{2}, \chi\frac{e}{2} - e, (1-\chi)e, (1-\chi)e\right]^T, \tag{2}$$

$$\mathbf{Q}_- = \left[\chi\frac{e}{2} - e, \chi\frac{e}{2}, \chi\frac{e}{2} - e, \chi\frac{e}{2}, (1-\chi)e, (1-\chi)e\right]^T, \tag{3}$$

and

$$\mathbf{Q}_{NULL} = \left[\chi\frac{e}{2}, \chi\frac{e}{2}, \chi\frac{e}{2}, \chi\frac{e}{2}, -e\chi, -e\chi\right]^T. \tag{4}$$

4.2 Configuration Energies

Intracellular energies, E_κ^{intra}, are computed using simple electrostatics as

$$E_\kappa^{\text{intra}} = \frac{1}{4\pi\epsilon_0}\sum_{i=0}^{4}\sum_{j=i+1}^{5}\frac{Q_\kappa(i)Q_\kappa(j)}{|\mathbf{r}(i) - \mathbf{r}(j)|}, \tag{5}$$

where $\kappa = \{+, -, NULL\}$ and the indices i and j represent the different sites of the cell. The interaction between states in neighbouring cells is pre-calculated based on a fully polarized neighbour. Throughout the simulation, the potential energy, $V_i^{(\text{ACTIVE})}$, induced by the intercellular interactions at each of the six sites of the cell is determined according to the following

$$V_i^{(\text{ACTIVE})} = \sum_{j\in\mathbf{N}} P_j V_{i,j}^{ACTIVE}, \tag{6}$$

where $V_{i,j}^{ACTIVE}$ is the potential at site i from cell j in a fully polarized configuration. P_j is the polarization of cell j. The relevant neighbourhood of cell i is given by the set $\mathbf{N}$ containing all cells which have a distance from cell i less than a user-defined parameter called the *radius of effect*. The potential energy contribution from the NULL state in neighbouring cells is

$$V_i^{(NULL)} = \sum_{j\in\mathbf{N}}(1 - |P_j|)V_{i,j}^{NULL}. \tag{7}$$

At each site we must also add the potential energy from the clocking electrodes

$$V_i^{(\text{clock})} = \sum_{j\in\boldsymbol{\Phi}} V_{i,j}^{(\text{electrode})}, \tag{8}$$

where $V_{i,j}^{(\text{electrode})}$ is the potential at site i with respect to the electrode j and Φ is the set of all electrodes in the design. The total potential energy is thus given as

$$V_i = V_i^{(\text{ACTIVE})} + V_i^{(NULL)} + V_i^{(\text{clock})}, \tag{9}$$

from which we can determine the electrostatic energy of each of the three basis configurations as

$$E_\kappa = E_\kappa^{\text{intra}} + \sum_{i=0}^{5} V_i Q_\kappa(i). \tag{10}$$

5 Cell Dynamics

The Hamiltonian for each cell is given as

$$\hat{H} = \begin{bmatrix} E_+ & 0 & -\gamma \\ 0 & E_- & -\gamma \\ -\gamma & -\gamma & E_{NULL} \end{bmatrix}, \tag{11}$$

where γ is the hopping energy between the ACTIVE states and the NULL state and depends on the nature of the molecular ligand coupling the redox sites of the molecule (the dots). No transition is permitted directly between the two ACTIVE states since hopping is only permitted between one of the top sites and the site at the bottom. The dynamics of each cell is determined using a 3-state coherence vector or generalized Bloch vector [17] and non-elastic interactions are incorporated through a relaxation time approximation as described in [15].

As explained in [15], the Hamiltonian of each cell can be projected onto the generators of $SU(3)$ as

$$\mathbf{\Gamma}_i = \frac{\text{Tr}\{\hat{H}\hat{\lambda}_i\}}{\hbar}, \tag{12}$$

where each of the generators, $\hat{\lambda}_i$, can be constructed using transition operators, $\hat{P}_{i,j} = |i\rangle\langle j|$, as

$$\begin{aligned}
\hat{\lambda}_1 &= \hat{P}_{1,2} + \hat{P}_{2,1}, \\
\hat{\lambda}_2 &= \hat{P}_{1,3} + \hat{P}_{3,1}, \\
\hat{\lambda}_3 &= \hat{P}_{2,3} + \hat{P}_{3,2}, \\
\hat{\lambda}_4 &= i(\hat{P}_{1,2} - \hat{P}_{2,1}), \\
\hat{\lambda}_5 &= i(\hat{P}_{1,3} - \hat{P}_{3,1}), \\
\hat{\lambda}_6 &= i(\hat{P}_{2,3} - \hat{P}_{3,2}), \\
\hat{\lambda}_7 &= \hat{P}_{2,2} - \hat{P}_{1,1}, \\
\hat{\lambda}_8 &= -\tfrac{1}{\sqrt{3}}(\hat{P}_{1,1} + \hat{P}_{2,2} - 2\hat{P}_{3,3}).
\end{aligned}$$

The explicit form of the Hamiltonian in this basis is

$$\begin{aligned}
\mathbf{\Gamma} = \tfrac{1}{\hbar}\Big[&0, -2\gamma, -2\gamma, 0, 0, 0, E_{(-)} - E_{(+)}, \\
&\tfrac{2}{\sqrt{3}}\left(E_{(NULL)} - \tfrac{E_{(-)}}{2} - \tfrac{E_{(+)}}{2}\right)\Big].
\end{aligned} \tag{13}$$

Including dissipation into the environment, the time-dependence of the coherence vector, which is a representation of the state of each cell in this basis of generators, is given by the Bloch equation with damping,

$$\frac{\partial}{\partial t}\boldsymbol{\lambda} = \mathbf{\Gamma} \times \boldsymbol{\lambda} - \frac{1}{\tau}[\boldsymbol{\lambda} - \boldsymbol{\lambda}_{SS}], \tag{14}$$

where λ_{SS} is the steady-state coherence vector, and τ is the relaxation time of the cell. The polarization of the cell can be determined using,

$$P_i = -\lambda_7. \tag{15}$$

The steady state coherence vector is

$$\boldsymbol{\lambda}_{SS}^{(j)} = \mathrm{Tr}\{\hat{\rho}_{SS}(t)\boldsymbol{\lambda}_j\}, \tag{16}$$

which is a projection of the steady-state density matrix,

$$\hat{\rho}_{SS}(t) = \frac{e^{-\hat{H}(t)/k_BT}}{\mathrm{Tr}\{e^{-\hat{H}(t)/k_BT}\}}, \tag{17}$$

onto the generators of $SU(3)$.

Our current implementation of this model uses Euler's method to solve equation (14). In each time-step of the algorithm, the potentials from all neighboring cells along with the potential induced by the clocking electrodes are updated and time is stepped forward by a user-defined time step, Δt.

6 Electrodes

As an initial approximation, the clocking electrodes are modelled as micro-strips, all of which are located on a layer separated from a ground plane that covers the entire circuit. The cells are located on their own layer very near to the ground plane to ensure that the field is near vertical at the level of the cells. The choice of these distances is detailed in Sec. 7.

The individual electrodes are divided up into a grid. At the centre of each grid square a time-dependent point charge is placed with charge $Q(t) = CV(t)/M$, where M is the total number of grid squares, and $V(t)$ is the potential applied to the entire electrode. The potential at a particular dot of the cell from an electrode is approximated using these point charges as

$$V_{i,j}^{(\mathrm{electrode})} = \frac{1}{4\pi\epsilon_0\epsilon_r}\sum_{i=0}^{M}\left(\frac{Q(t)}{|r_i - r_j|} - \frac{Q(t)}{|\mathbf{r}_i - \mathbf{r}_j + \mathbf{r}_{\mathrm{image}}|}\right) \tag{18}$$

where $\mathbf{r}_{\mathrm{image}}$ is the vector from the charge to its associated mirror image charge directly above the ground plane. This method of images ensures a zero potential everywhere on the ground plane. These simplifications are insufficient to provide accurate predictions of the switching potential. A far more accurate approach using a finite-element method would provide a better estimate for switching potentials accounting, for example, for the non-uniform distribution of charge on the electrodes. However, these initial simplifications are believed to be sufficient to demonstrate the proof-of-concept since we are focussing on the circuit-level behavior.

7 Simulation

Fig. 6 shows the QCA layout used in our simulations. The bold rectangular boxes illustrate the outlines of the submerged electrodes. The ground plane is not shown. A sinusoidal signal is used to emulate an external input. The inverter is realized by a 180-degree phase shift in the applied signal to Gate Electrode 2 from that applied to Gate Electrode 1. The frequency of the applied input is one quarter of the frequency applied to clocking electrodes E1-E3. Fixed polarization cells are explicitly included at each arm of the structure and maintain their polarization throughout the simulation. Three cells at the leg of the "T" structure represent the output cells and their polarization is recorded throughout the simulation.

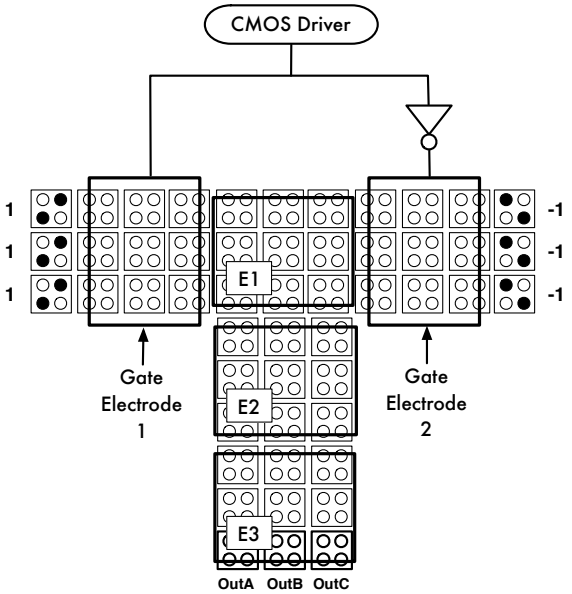

Fig. 6 Proposed input driver layout used in the numerical simulations.

Each of the cells in the circuit has a bounding box with width and length of 5 nm, a height of 3 nm and were separated by 1 nm. The dot-dot distance is 2.5 nm. The interaction energy (kink energy) between cells for this cell size and spacing is 46.5 meV. The tunneling energy between each cell, γ, was set to 3.7 eV to ensure strong polarization. Total simulation time was set at $t = 0.16$ ns, using a time step, $\Delta t = 2 \times 10^{-16}$ s, and a relaxation time, $\tau = 2 \times 10^{-15}$ s. The neutralizing charge was located in the bottom two sites of each cell, *i.e.*, $\chi = 0$, implementing cells that are normally off,

The two gate electrodes are 14.5 nm × 20 nm in size and are divided into a grid of 10 × 30. The clocking electrodes are 18 nm × 14.5 nm in size and are divided into a grid of 20 × 10. The entire circuit including electrodes could be scaled up to wider interconnects at a cost of computational time without sacrificing the functionality of the input driver. The electrodes were placed 10 nm below the ground plane, and all cells

were placed 7 nm above the electrodes. A 5 V sinusoid with a frequency of 50 GHz was applied to electrodes E1-E3 with a relative phase of 90° to create a forward moving wave that propagates the input to the output. The relative permittivity, ϵ_r, of the surrounding material was assumed to be 12.9, and 1.0 between cells. The simulation temperature was 150K.

8 Results

Simulation results for the input configuration are shown in Fig. 7. The simulation emulates an input that is alternating between $P = -1$ and $P = 1$ at a frequency of 12.5 GHz. It is clear from these results that the output is able to correctly follow the input signal. The apparent phase shift between the input and output results from the delay through the output leg. While it is understood that the intrinsic switching speed of cells may be high, the circuit speed will ultimately be limited by the input driver and the switching speed of the electrodes rather than the cells, which may have switching speeds on the order of THz [19]. Thus, the frequencies used in these simulations are consistent with current [20] and expected [19] speed performances of standard CMOS circuits.

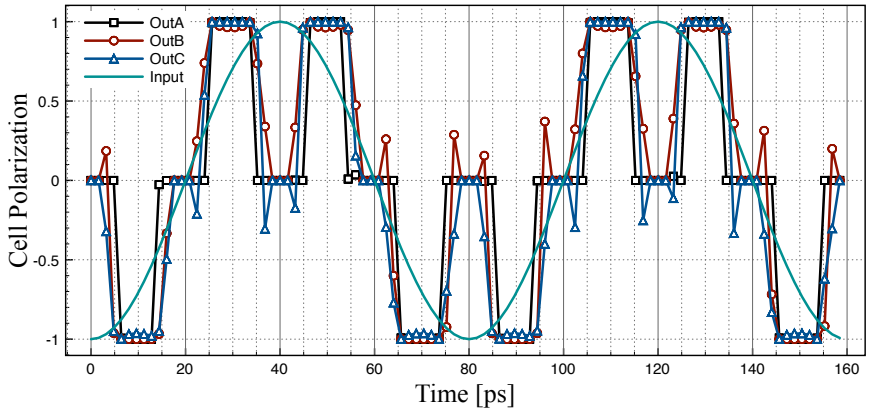

Fig. 7 Simulation results for the proposed input driver configuration

9 Conclusions

A novel architecture, enabling an external logic input to be fed into a molecular QCA circuit is proposed. The input is converted to a control potential on two separate gating electrodes. These electrodes gate the polarization from two fixed-polarization cell clusters to three clocking zones that propagate the input into the QCA circuit. Using the coherence vector formalism, a finite-state model was implemented to simulate and validate the operation of this input driver. This approach overcomes the problem of input without the need for any additional structures. The electrodes and fixed polarization cells used in this proposal are required for the basic operation of a QCA circuit

and are not unique to this proposal. In addition, no direct connection is required to individual QCA cells and interconnects can be much wider than one cell, potentially simplifying the fabrication. Alternative input schemes that have already been applied to metallic-island and semiconductor QCA are not applicable here since they depend on the ability to modify the potential of the individual dots, an approach that would be difficult with molecular cells.

References

1. M. Lieberman, S. Chellamma, B. Varughese, Y. L. Wang, C. Lent, G. H. Bernstein, G. Snider, and F. C. Peiris, "Quantum-dot cellular automata at a molecular scale," *Molecular Electronics II*, vol. 960, pp. 225–239, 2002.
2. C. S. Lent, "Molecular electronics - bypassing the transistor paradigm," *Science*, vol. 288, no. 5471, pp. 1598–1599, 2000.
3. C. S. Lent, P. D. Tougaw, W. Porod, and G. H. Bernstein, "Quantum cellular automata," *Nanotechnology*, vol. 4, pp. 49–57, 1993.
4. Y. H. Lu and C. S. Lent, "A metric for characterizing the bistability of molecular quantum-dot cellular automata," *Nanotechnology*, vol. 19, no. 15, pp. –, 2008.
5. Y. Lu, M. Liu, and C. Lent, "Molecular quantum-dot cellular automata: From molecular structure to circuit dynamics," *Journal of Applied Physics*, vol. 102, no. 3, pp. 034311–7, 2007.
6. L. Yuhui, L. Mo, and C. Lent, "Molecular electronics - from structure to circuit dynamics," in *6th IEEE Conference on Nanotechnology*, vol. 1, pp. 62–65, 2006.
7. L. Yuhui and C. S. Lent, "Theoretical study of molecular quantum dot cellular automata," in *10th International Workshop on Computational Electronics*, pp. 118–119, 2004.
8. W. C. Hu, K. Sarveswaran, M. Lieberman, and G. H. Bernstein, "High-resolution electron beam lithography and DNA nano-patterning for molecular QCA," *Ieee Transactions on Nanotechnology*, vol. 4, no. 3, pp. 312–316, 2005.
9. H. Qi, S. Sharma, Z. H. Li, G. L. Snider, A. O. Orlov, C. S. Lent, and T. P. Fehlner, "Molecular quantum cellular automata cells. Electric field driven switching of a silicon surface bound array of vertically oriented two-dot molecular quantum cellular automata," *Journal of the American Chemical Society*, vol. 125, no. 49, pp. 15250–15259, 2003.
10. K. Walus and G. A. Jullien, "Design tools for an emergng SoC technology: Quantum-dot cellular automata," *Proceedings of the IEEE*, vol. 94, no. 6, pp. 1225–1244, 2006.
11. K. Hennessy and C. S. Lent, "Clocking of molecular quantum-dot cellular automata," *Journal of Vacuum Science & Technology B*, vol. 19, no. 5, pp. 1752–1755, 2001.
12. E. P. Blair and C. S. Lent, "An architecture for molecular computing using quantum-dot cellular automata," in *3rd IEEE Conference on Nanotechnology*, vol. 1, pp. 402–405 vol.2, 2003.
13. C. S. Lent and B. Isaksen, "Clocked molecular quantum-dot cellular automata," *IEEE Transactions on Electron Devices*, vol. 50, no. 9, pp. 1890–1896, 2003.
14. K. Walus, G. Schulhof, and G. A. Jullien, "Implementation of a simulation engine for clocked molecular QCA," in *Canadian Conference on Electrical and Computer Engineering*, pp. 2128–2131, 2006.
15. J. Timler and C. S. Lent, "Maxwell's demon and quantum-dot cellular automata," *Journal of Applied Physics*, vol. 94, no. 2, pp. 1050–1060, 2003.
16. C. S. Lent, M. Liu, and Y. H. Lu, "Bennett clocking of quantum-dot cellular automata and the limits to binary logic scaling," *Nanotechnology*, vol. 17, no. 16, pp. 4240–4251, 2006.
17. G. Mahler and V. A. Weberrüs, *Quantum Networks: Dynamics of Open Nanostructures*. Berlin, Germany: Springer-Verlag, 1998.
18. K. Walus, T. J. Dysart, G. A. Jullien, and R. A. Budiman, "QCADesigner: a rapid design and simulation tool for quantum-dot cellular automata," *Nanotechnology, IEEE Transactions on*, vol. 3, no. 1, pp. 26–31, 2004.
19. J. Timler and C. S. Lent, "Power gain and dissipation in quantum-dot cellular automata," *Journal of Applied Physics*, vol. 91, no. 2, pp. 823–831, 2002.
20. H. Tamura, M. Kibune, H. Yamaguchi, K. Kanda, K. Gotoh, H. Ishida, and J. Ogawa, "Circuits for CMOS high-speed I/O in sub-100 nm technologies," *IEICE Trans. Electron.*, vol. E89, no. 3, pp. 300–311, 2006.